Charge Sensing the Parity of an Andreev Molecule

David van Driel,[1] Bart Roovers,[1] Francesco Zatelli,[1] Alberto Bordin,[1] Guanzhong Wang,[1]
Nick van Loo,[1] Jan Cornelis Wolff,[1] Grzegorz P. Mazur,[1] Sasa Gazibegovic,[2] Ghada Badawy,[2]
Erik P.A.M. Bakkers,[2] Leo P. Kouwenhoven,[1,*] and Tom Dvir[1]

[1] *QuTech and Kavli Institute of NanoScience, Delft University of Technology, 2600 GA Delft, Netherlands*
[2] *Department of Applied Physics, Eindhoven University of Technology, 5600 MB Eindhoven, Netherlands*

(Received 6 November 2023; revised 2 February 2024; accepted 23 February 2024; published 1 April 2024)

The proximity effect of superconductivity on confined states in semiconductors gives rise to various bound states such as Andreev bound states, Andreev molecules, and Majorana zero modes. While such bound states do not conserve charge, their fermion parity is a good quantum number. One way to measure parity is to convert it to charge first, which is then sensed. In this work, we sense the charge of Andreev bound states and Andreev molecules in an InSb-Al hybrid nanowire using an integrated quantum dot operated as a charge sensor. We show how charge sensing measurements can resolve the even and odd states of an Andreev molecule, without affecting the parity. Such an approach can be further used for parity measurements of Majorana zero modes in Kitaev chains based on quantum dots.

DOI: 10.1103/PRXQuantum.5.020301

I. INTRODUCTION

Majorana zero modes (MZMs) are predicted to appear at the ends of a 1D chain of spin-polarized, electronic sites with superconducting pairing [1–3], which can be implemented with use of quantum dots (QDs) coupled to superconductors [4,5]. Even a minimal, two-site Kitaev chain hosts MZMs in a parameter sweet spot [6–8], and was recently realized in a semiconductor-superconductor hybrid nanowire [9]. MZMs in Kitaev chains are predicted to be robust with regard to local perturbations and to obey non-Abelian statistics, allowing the demonstration of Ising anyon fusion rules and braiding [10,11]. Qubit states can be encoded in the parity of pairs of MZMs, making parity readout crucial for any quantum information experiment involving MZMs. Proposed readout techniques include circuit quantum electrodynamics [12,13], quantum capacitance measurements [14], and charge sensing [15]. To read out parity with a charge measurement, it must first be converted into charge, and then sensed [16]. Although charge sensing has been applied to semiconductor-superconductor hybrids before, it has never been used to detect fractional charge differences [17,18]. This can potentially be necessary for parity readout in Kitaev chains, given that the charge difference between the even ground state and the odd ground state can range from 0 to $1e$. In this work, we present charge sensing measurements of a hybrid semiconductor-superconductor system. First, we measure the charge of an Andreev bound state (ABS) in its even and odd fermion parity ground states. Then, we couple a QD to an ABS to form an Andreev molecule, and we infer its ground state parity from tunnel spectroscopy and charge sensing measurements. As opposed to transport, charge sensing does not alter the parity itself, highlighting its potential as a tool for MZM parity readout in Kitaev chains.

II. RESULTS

A. Device characterization

Figure 1(a) shows an SEM image of the device measured in this work. An InSb nanowire is placed on a thin layer of gate dielectric, below which are finger gates (see Refs. [19,20] for details on device fabrication). The middle section of the wire, the hybrid segment, is contacted by a grounded Al thin film and hosts ABSs. We define a QD to the left of the hybrid segment by setting V_{LO} and V_{TL} to create tunnel junctions in the nanowire. We control the QD's electrochemical potential using V_{CS} and operate it as a single lead QD charge sensor (CS) [21]. The tunnel gate between the CS and the hybrid segment is kept at a negative voltage ($V_{\mathrm{TL}} = -100\,\mathrm{mV}$) to fully quench transport and ensure their coupling is only capacitive. The nanowire section to the right of the hybrid segment can be

---

[*] l.p.kouwenhoven@tudelft.nl

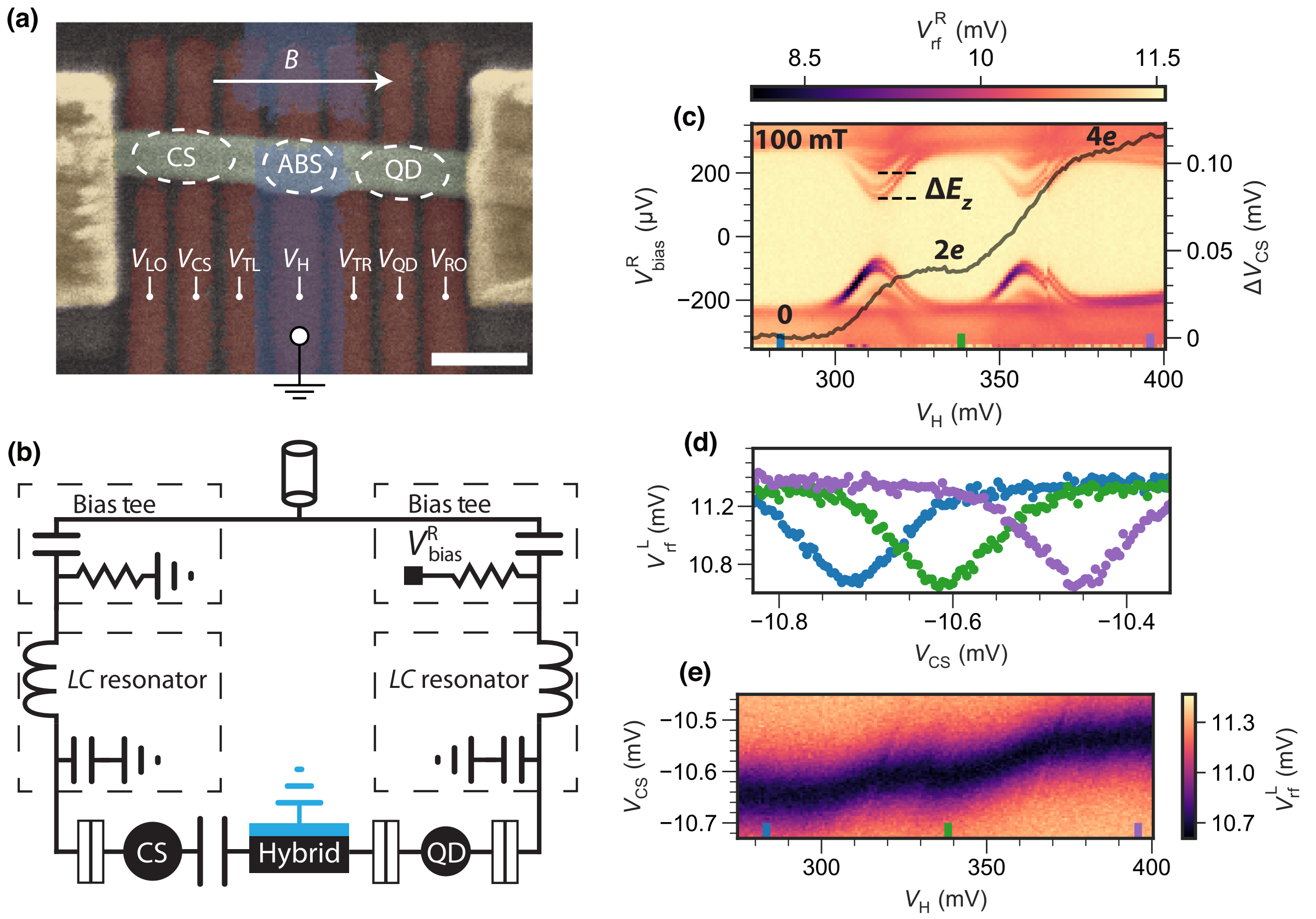

FIG. 1. Device setup and characterization. (a) False-color SEM micrograph of our device. An InSb nanowire (green) is placed on an array of bottom gates (brown) and contacted by normal Cr/Au leads (yellow). We define a QD to the left of the hybrid segment, and operate it as a CS. Another QD can be formed with the gates to the right of the hybrid segment. The white markers and their corresponding text indicate the electrostatic gates to which a voltage is applied. The scale bar is 200 nm. (b) dc equivalent circuit of our device. Both normal leads of the hybrid segment are connected to off-chip *LC* resonators, which are multiplexed. Each *LC* resonator has a bias tee that can be used to bias the leads with respect to the grounded Al. (c) Amplitude of the reflected rf signal of the right lead V^R_{rf} for varying voltage on the hybrid plunger gate V_H and the right bias V^R_{bias} for external magnetic field $B = 100$ mT, $V_{TR} = 0$, $V_{QD} = 500$ mV, and $V_{RO} = 500$ mV. The superimposed line corresponds to a shift of the gate voltage corresponding to the Coulomb resonance of the CS ΔV_{CS} for each V_H setting, extracted from (e). The Zeeman splitting of the first ABS is indicated by ΔE_Z. 0, 2*e*, and 4*e* indicate additional charge accumulated on the hybrid. (d) Amplitude of the reflected rf signal of the left lead V^L_{rf} for varying voltage on the CS plunger gate V_{CS} at fixed values of V_H indicated by the colored bars in (c),(e). (e) V^L_{rf} for varying V_{CS} and V_H.

either a tunnel barrier or a QD, depending on the tunnel gate voltages V_{RO} and V_{TR}.

The nanowire is contacted by two normal Cr/Au leads that can be used for dc transport and radio-frequency (rf) reflectometry measurements. Figure 1(b) shows the dc equivalent circuit of the device and its connections. Both normal leads are connected to *LC* resonators with bias tees, allowing us to independently voltage bias them with respect to the grounded Al. The *LC* resonators are off-chip and multiplexed (see Ref. [22] for details). Further details on the reflectometry circuit can be found in Ref. [23]; for resonator characterization, see Appendix A. Experiments are performed in a dilution refrigerator at a base temperature of 30 mK.

B. ABS even ground state charge

The hybrid segment hosts ABSs that can have an odd, doublet ground state ($\{|\downarrow\rangle, |\uparrow\rangle\}$) or an even ground state. We consider an ABS in the atomic limit, where the even ground state is a singlet: $|S\rangle = u\,|0\rangle - v\,|2\rangle$, with 0 and 2 denoting the occupation of a single orbital [24,25]. The singlet state changes between being mostly unoccupied (0-like) and doubly occupied (2-like) when the electrochemical potential of the ABS changes. Note that this is a gradual change of the ground state, as opposed to changing a QD ground state by occupying additional electrons. When the semiconductor-superconductor coupling is stronger than the charging energy, the ABS has an even ground state with a doublet excited state [26].

To characterize the hybrid segment, we set $V_{\mathrm{RO}} = 500\,\mathrm{mV}$ and $V_{\mathrm{QD}} = 500\,\mathrm{mV}$ to accumulate electrons, and we create a tunnel barrier by setting $V_{\mathrm{TR}} = 0\,\mathrm{mV}$ to perform tunneling spectroscopy from the right lead. Figure 1(c) shows the amplitude of the reflected rf signal of the right lead $V_{\mathrm{rf}}^{\mathrm{R}}$ for varying hybrid plunger gate voltage V_{H} and right voltage bias $V_{\mathrm{bias}}^{\mathrm{R}}$. A dip in $V_{\mathrm{rf}}^{\mathrm{R}}$ can be related to a peak in differential conductance [23]. The hybrid segment has a hard-gapped density of states with two well-separated ABSs, the energy of which can be controlled with V_{H}. Each ABS excitation is split into two resonances, because we apply 100 mT along the nanowire axis. From the Zeeman splitting $\Delta E_Z = 80\,\mu\mathrm{eV}$, we obtain an effective g factor of 13.8 for the ABS. The ABS excitations do not cross zero bias, signaling an even ground state for the entire V_{H} range. We note that there is a switch in the signal at $V_{\mathrm{H}} \approx 365\,\mathrm{mV}$, which we attribute to a charge jump in the hybrid segment.

Figure 1(d) shows the amplitude of the reflected rf signal of the left lead $V_{\mathrm{rf}}^{\mathrm{L}}$ for varying plunger gate voltage of the CS V_{CS}, taken at three different values of V_{H}. A Coulomb resonance of the CS is seen as a dip in $V_{\mathrm{rf}}^{\mathrm{L}}$ whenever a CS level is aligned with the Fermi level of the left lead [27]. We see that the V_{CS} value corresponding to the $V_{\mathrm{rf}}^{\mathrm{L}}$ minimum changes due to V_{H}, which has two possible causes. First, V_{H} directly gates the CS due to cross-capacitance. Second, V_{H} can change the occupation of the hybrid segment and the resulting charge is sensed by the CS. To extract the charge sensing signal only, we define virtual gates that are linear combinations of the physical gate voltages, to compensate for cross-capacitances between gates (for details, see Appendix B).

In Fig. 1(e), we show one particular CS Coulomb resonance for varying V_{CS} and V_{H}. We have subtracted a global slope from the data, which we attribute to imperfect virtual gate settings. The global slope was chosen such that the CS resonance is roughly constant in V_{H} up to 300 mV, for which there are no subgap states (for details and raw data, see Appendix B). We note the presence of switches in the CS signal at $V_{\mathrm{H}} = 320\,\mathrm{mV}$ and $V_{\mathrm{H}} = 365\,\mathrm{mV}$. The latter switch occurs at the same V_{H} value as the one observed in Fig. 1(c). We attribute the switches in the CS signal to charge jumps in the hybrid segment (for more discussion, see Appendix C).

The superimposed black line in Fig. 1(c) shows the shift of the CS Coulomb resonance ΔV_{CS} as found from Fig. 1(e). We see that ΔV_{CS} depends on V_{H} and changes most strongly when there is an ABS at subgap energies. The absence of sharp jumps in ΔV_{CS} shows that there are no abrupt changes of charge, which is consistent with an even ground state for the entire V_{H} range as found from Fig. 1(c). We interpret the change in ΔV_{CS} at $V_{\mathrm{H}} = 310\,\mathrm{mV}$ and $V_{\mathrm{H}} = 360\,\mathrm{mV}$ as the CS sensing the charge of the ABSs changing continuously from 0 to $2e$, where e is the charge of the electron.

Gradual change of charge without change of parity, as seen here, has been observed before in normal double quantum dots [28,29]. In our case, however, the ABS exchanges charge with a large Al reservoir and becomes a coherent superposition of 0 and $2e$.

C. Single ABS parity readout

To use our charge sensor for parity readout, we focus on an ABS with a ground state that can be changed from even to odd parity with use of V_{H}. Figure 2(a) shows the spectrum of such an ABS in a V_{H} range different from the range in Fig. 1 for $B = 0\,\mathrm{mT}$. We see a subgap state that crosses zero energy twice for changing V_{H}, giving rise to a characteristic ABS eye shape [30,31]. The ABS ground state between the zero-energy crossings is a spin doublet $|D\rangle = |{\downarrow}\rangle\,, |{\uparrow}\rangle$ [26]. Having a doublet ground state at $B = 0\,\mathrm{mT}$ signals that the ABS has a charging energy that is non-negligible. We note that this is uncommon among most ABSs in the hybrid segment, as can be seen from measurements in a larger V_{H} range (see Appendix D). We choose this particular ABS as it allows us to measure charge in both the even ground state and the odd ground state. Figures 2(b) and 2(c) show spectra of the ABS at $B = 100\,\mathrm{mT}$ and $B = 250\,\mathrm{mT}$, respectively. The magnetic field Zeeman-splits the doublet states, making the odd state lower in energy than the even state over a larger V_{H} range.

In Fig. 2(d) we show the processed shift of the CS Coulomb resonance ΔV_{CS} for varying V_{H} at different B values. To obtain ΔV_{CS} for each B value, we first set the CS on Coulomb resonance using V_{CS} and measure $V_{\mathrm{rf}}^{\mathrm{L}}$ for varying V_{H}. We then convert the measured $V_{\mathrm{rf}}^{\mathrm{L}}$ to the corresponding shift of the CS Coulomb resonance, resulting in ΔV_{CS}. For details, see Appendix E.

For each B value, we identify three distinct V_{H} regions where the ΔV_{CS} response is roughly flat. The middle region of these at $V_{\mathrm{H}} \approx 260\,\mathrm{mV}$ occupies a larger V_{H} range for increasing B. This is consistent with $|{\downarrow}\rangle$ being the ground state for a larger V_{H} range, as inferred from Figs. 2(a)–2(c) [note that the V_{H} values for which the ABS has an odd ground state differ slightly between Figs. 2(a)–(c) and Fig. 2(d) due to different V_{LO} and V_{TL} gate voltages, which were chosen to optimize the sensitivity of the charge sensor]. We interpret the three distinct ΔV_{CS} values for increasing V_{H} as corresponding to the 0-like even, singly occupied odd, and 2-like even states of the ABS.

We observe finite curvature in ΔV_{CS} for the even ground state, which we attribute to mixing of the 0 and 2 occupations, similarly to what is seen in Fig. 1(e). The curvature is most visible close to the even-odd transition, and becomes less apparent with increasing B. At $B = 0\,\mathrm{mT}$, the even-odd transition (indicated by the blue arrow) occurs when the ABS is near its energy minimum, where the average ABS charge is $1e$ for both the even state and the odd state

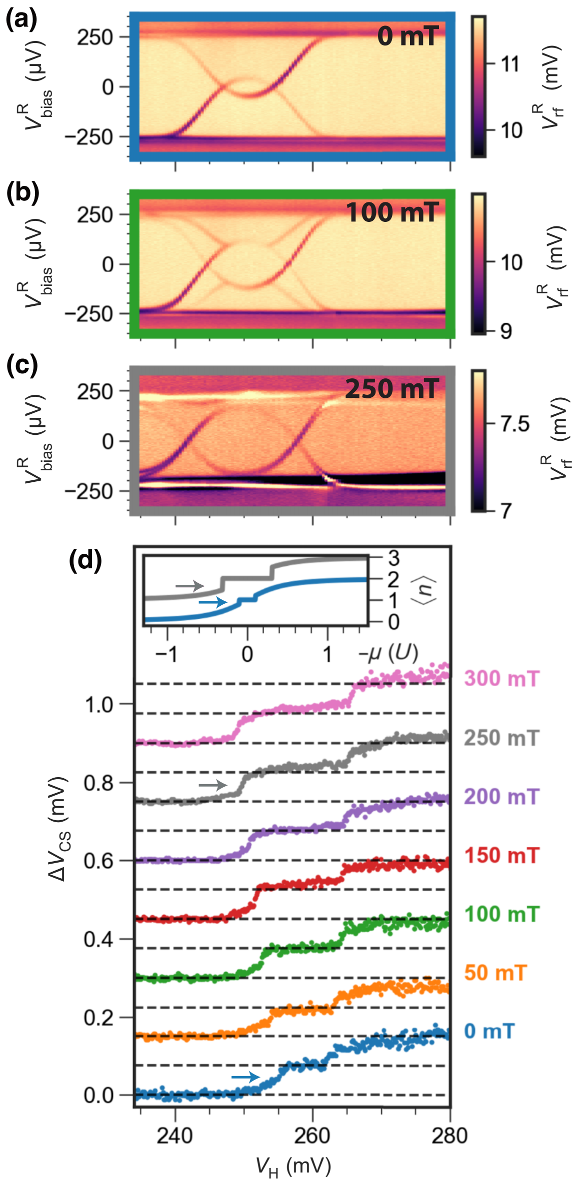

FIG. 2. Charge sensing the even and odd ground states of an ABS. (a)–(c) Amplitude of the reflected rf signal of the right lead $V_{\mathrm{rf}}^{\mathrm{R}}$ for varying hybrid gate voltage V_{H} and right bias $V_{\mathrm{bias}}^{\mathrm{R}}$ recorded at (a) $B = 0$ mT, (b) $B = 100$ mT, and (c) $B = 250$ mT for $V_{\mathrm{TR}} = 0$ mV, $V_{\mathrm{TL}} = -100$ mV, $V_{\mathrm{LO}} = 170$ mV, and $V_{\mathrm{RO}} = 500$ mV. (d) Shift of the CS Coulomb resonance ΔV_{CS} at different B values for $V_{\mathrm{TL}} = -140$ mV and $V_{\mathrm{LO}} = 172$ mV. The horizontal lines are offset by 75 μV, which corresponds to a charge difference of approximately $1e$. The arrows indicate the even-odd transition at $B = 0$ mT and $B = 250$ mT, respectively. The inset shows the occupation expectation value of the ABS ground state $\langle n\rangle$ for varying chemical potential μ at different B values, calculated in the atomic limit. The arrows indicate the even-odd transition.

[32,33]. The charge of the even state gradually changes from 0 to almost $1e$ in the V_{H} range before the transition. At $B = 250$ mT, the even-odd transition occurs when the ABS is no longer close to its energy minimum. The difference in charge between the even state and the odd state is then greater, resulting in a sharper change of ΔV_{CS}, as indicated by the gray arrow.

If the curvature of ΔV_{CS} is exclusive to the even ground state, we can use it to infer the parity of the ABS using charge sensing only. To illustrate this point, we calculate and show the charge of an ABS in the inset in Fig. 2(d). Here, the average occupation $\langle n\rangle$ is shown for varying chemical potential μ at two different values of B (for more details, see Appendix F). At low B, curvature in $\langle n\rangle$ is a characteristic sign of an ABS in a singlet ground state, provided that the parent gap is much larger than the charging energy. To infer the ABS parity from the curvature of ΔV_{CS} experimentally, the ABS cannot be strongly coupled to another discrete state or orbital. In the coupled system, changing the gate voltage can transfer charge between the states. This can result in curvature of ΔV_{CS} for the odd ground state in addition to the even one.

So far, we have established that charge sensing measurements can resolve the charge differences between the even ground state and the odd ground state of a single ABS. In a two-site Kitaev chain, however, it is the combined parity of two hybridized QDs that has to be detected. We create a proxy system by hybridizing a QD with an ABS and charge sense it to give a minimal demonstration of parity readout for Kitaev chains. Parity readout of Majorana zero modes requires extra steps, which we detail in the discussion. We note that an alternating ABS-QD array can also constitute a Kitaev chain [34,35].

D. Andreev molecule spectroscopy

To create the ABS-QD system, we define a QD to the right of the hybrid segment by creating a tunnel barrier using V_{RO} [see Fig. 1(a)]. We then lower the tunnel barrier between the QD and the hybrid segment by increasing V_{TR}.

Figure 3(a) shows a charge stability diagram measured in $V_{\mathrm{rf}}^{\mathrm{R}}$ for varying V_{H} and QD plunger gate voltage V_{QD}. We see avoided crossings that indicate hybridization of the QD and ABS. The QD resonance can be seen when the ABS is off resonance (blue bar), which we attribute to local Andreev reflection on the QD and the use of rf reflectometry instead of differential conductance (for details, see Appendix G). Similarly, the ABS can be observed when the QD is off resonance (e.g., red bar). Because of the strong hybridization between the QD and the ABS, the latter can always be seen in spectroscopy on probing of the QD.

Figure 3(b) shows the ground state parity of a QD coupled to an ABS, computed in the atomic limit. States are indicated in the ABS-QD number basis, with $|S\rangle$ denoting the ABS singlet. We emphasize that the singlet is dominantly 0-like or 2-like at $-\tilde{\mu}_{\mathrm{ABS}} = \pm 1 U_{\mathrm{QD}}$. The avoided crossings have different sizes in Fig. 3(b), which

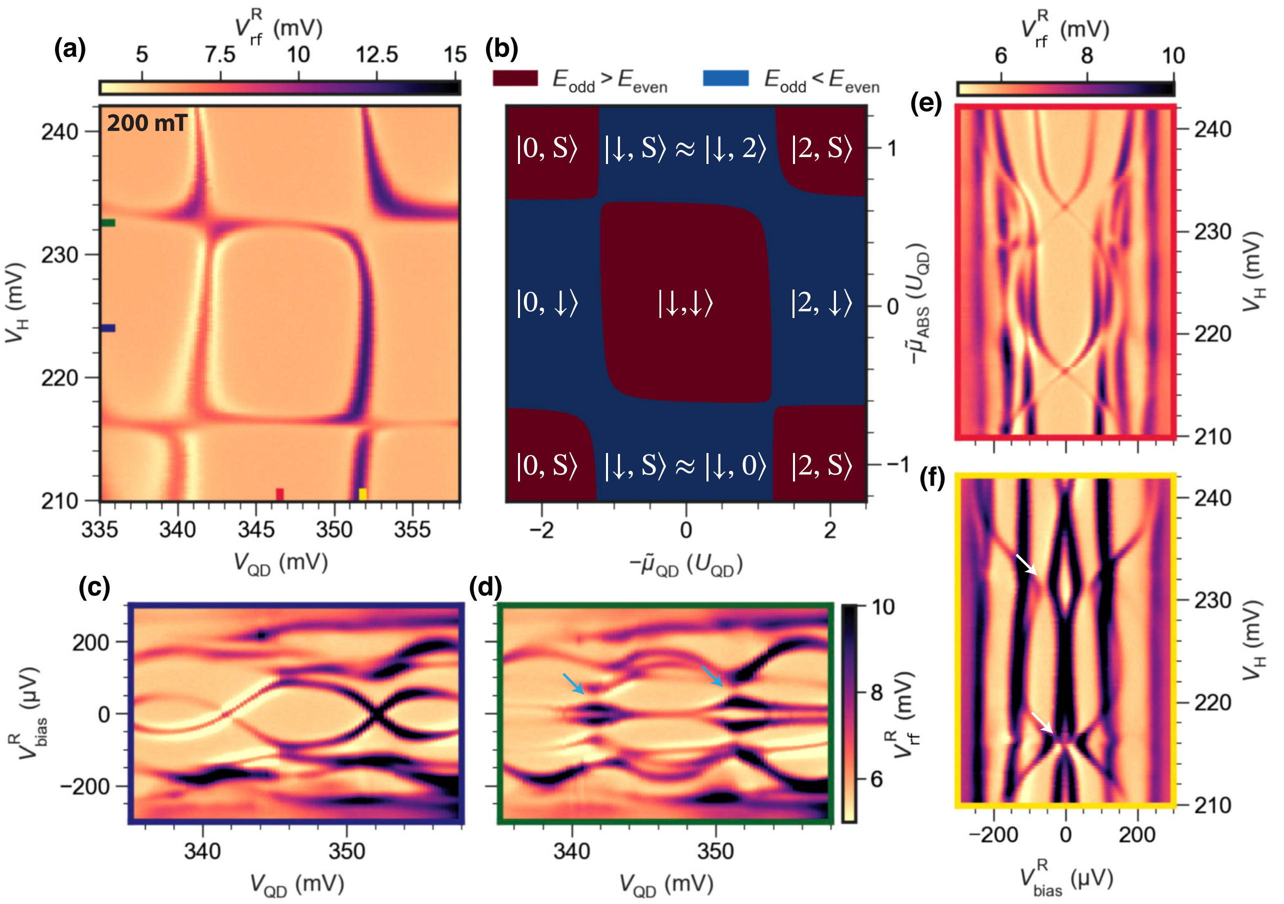

FIG. 3. Spectroscopy of a hybridized ABS-QD system. (a) Amplitude of the reflected rf signal of the right lead $V_{\mathrm{rf}}^{\mathrm{R}}$ for varying QD plunger gate voltage V_{QD} and V_{H} recorded at $V_{\mathrm{bias}}^{\mathrm{R}} = 0\,\mathrm{V}$, $B = 200\,\mathrm{mT}$, $V_{\mathrm{TR}} = 215\,\mathrm{mV}$, and $V_{\mathrm{RO}} = 340\,\mathrm{mV}$. (b) Parity of the lowest-energy eigenstate of a coupled ABS-QD system for varying QD and ABS chemical potential $\tilde{\mu}_{\mathrm{QD}}$ and $\tilde{\mu}_{\mathrm{ABS}}$, computed in the atomic limit. We designate the ground state parity as even if $E_{\mathrm{odd}} > E_{\mathrm{even}}$ and odd if $E_{\mathrm{odd}} < E_{\mathrm{even}}$. The superimposed text indicates the ground states in the $|N, M\rangle = |N\rangle_{\mathrm{QD}} \otimes |M\rangle_{\mathrm{ABS}}$ basis of the ABS-QD system. We denote the ABS singlet state by $|S\rangle$, and highlight its dominant occupation for the $|{\downarrow}, S\rangle$ state. (c),(d) $V_{\mathrm{rf}}^{\mathrm{R}}$ for varying V_{QD} and $V_{\mathrm{bias}}^{\mathrm{R}}$, recorded at two different values of V_{H} indicated by the horizontal blue and green bars in (a). (e),(f) $V_{\mathrm{rf}}^{\mathrm{R}}$ for varying V_{H} and $V_{\mathrm{bias}}^{\mathrm{R}}$, recorded at two different values of V_{QD} indicated by the vertical red and yellow bars in (a).

is caused by the mixing of 0 and 2 occupations of the ABS (for details on the model, see Appendix F). We see that Fig. 3(b) qualitatively reproduces most of the features of Fig. 3(a).

Figures 3(c) and 3(d) show spectra of the QD for varying V_{QD} and $V_{\mathrm{bias}}^{\mathrm{R}}$ at fixed values of V_{H} indicated by the horizontal lines in Fig. 3(a). When the ABS in the hybrid segment is not at zero energy [blue bar, Fig. 3(c)], we see multiple subgap states, where the lowest one forms a typical eye shape. This indicates the formation of Yu-Shiba-Rusinov (YSR) states on the QD, due to its strong coupling to the hybrid segment [36–40]. Figure 3(d) (green bar) shows the QD spectrum when the ABS excitation is at zero energy, i.e., on resonance. Here we see that the ABS and QD states form subgap bonding and antibonding states when they are on resonance, indicated by the blue arrows. Two hybridized subgap states are often referred to as an "Andreev molecule," which usually designates two coupled YSR states [41–47] or phase-tunable ABSs in Josephson junctions [48–50]. Because our ABS-QD system shows hybridization of an ABS in a hybrid with a YSR state in a QD, we categorize it as an Andreev molecule.

Figures 3(e) and 3(f) show spectra of the QD for varying V_{H} at fixed values of V_{QD} indicated by the vertical lines in Fig. 3(a). When the QD is off resonance [red bar, Fig. 3(e)] the lowest subgap state crosses zero energy twice, and the excited states are close in energy to the superconducting gap. Figure 3(f) (yellow bar) shows the spectrum when the QD excitation is at zero energy. When the ABS is on resonance, it splits the zero-bias peak of the QD, indicated by the white arrows. This effect is known to occur for QDs strongly coupled to ABSs [51–53].

E. Andreev molecule parity readout

Next, we sense the charge of the ABS within the ABS-QD system. Figure 4(a) shows the phase of the reflected rf signal of the left lead $\phi^{\mathrm{L}}_{\mathrm{rf}}$ for varying V_{QD} and V_{H} at different gate and field settings from Fig. 3. We set the CS on Coulomb resonance using V_{CS}, at the V_{QD} and V_{H} settings that correspond to the bottom-left corner of Fig. 4(a). Globally, we observe three horizontal regions where $\phi^{\mathrm{L}}_{\mathrm{rf}}$ depends almost only on V_{H}, which we interpret as the 0-like even, singly occupied $|\downarrow\rangle$, and 2-like even states of the ABS. In addition, there are four regions where $V^{\mathrm{L}}_{\mathrm{rf}}$ depends visibly on V_{QD}, which we attribute to the QD hybridizing with the ABS. These regions are highlighted with dashed rectangles.

In Fig. 4(b) we show an enlargement of Fig. 4(a) corresponding to the black rectangle. Here, the CS was gated to be on the steepest slope of the Coulomb peak with use of V_{CS} at the start of the measurement. We see an off-diagonal avoided crossing, which signals an interdot transition [54]. Because this is the first interdot transition of this QD orbital and ABS, we label the bottom-left corner of Fig. 4(b) with $|0, S\rangle$, where the QD orbital is unoccupied and the ABS is in the 0-like singlet state. The other states are labeled by our counting the added electrons. Although the QD is proximitized by coupling to the hybrid, as seen in Fig. 3(c), we retain the number basis for clarity.

Figure 4(c) shows the numerical derivative of Fig. 4(b), $d\phi^{\mathrm{L}}_{\mathrm{rf}}/dV_{\mathrm{QD}}$, after processing with a Savgol filter. The dips in $d\phi^{\mathrm{L}}_{\mathrm{rf}}/dV_{\mathrm{QD}}$ form two blue hyperbolas that indicate where the even and odd ground states are degenerate [29]. On the basis of the states inferred from Fig. 4(b), we label the region between the hyperbolas as odd (“O”) and the two areas outside as even (“E”).

Figure 4(d) shows a line-cut of $\phi^{\mathrm{L}}_{\mathrm{rf}}$ taken along the orange line in Fig. 4(b), where V_{QD} and V_{H} are changed in parallel, indicated by δ. The two vertical, dashed black lines correspond to the gate values of the superimposed crosses in Fig. 4(c), which we use to divide the range of δ into even and odd ground states. We note that there are three regions where $\phi^{\mathrm{L}}_{\mathrm{rf}}$ is roughly constant, and that these coincide with even and odd parity sectors. From this we conclude that we can read out the parity of the ABS-QD system by measuring its charge.

Extending parity readout using charge sensing to a two-site Kitaev chain requires an additional step however. In the “poor man’s Majorana” sweet spot, the degenerate even and odd parity ground states have the same charge [8]. Detuning one QD creates a charge difference between the even ground state and the odd ground state on the other QD, while the states remain degenerate [55]. A local charge sensing measurement on the nondetuned QD can then tell the parity on the basis of charge. This protocol of detuning and measuring charge has to be performed within the quasiparticle poisoning time, otherwise the parity flips during the measurement. We note that our rf integration

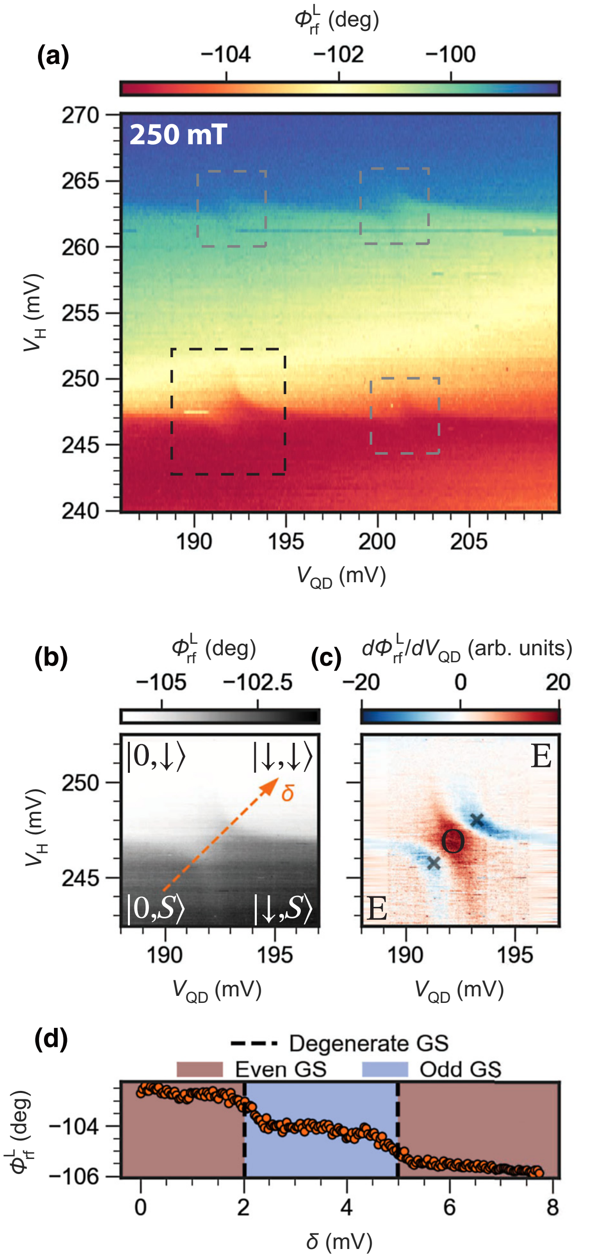

FIG. 4. Charge sensing measurements of the ABS-QD system. All data were recorded for $V_{\mathrm{TR}} = 255\,\mathrm{mV}$, $V_{\mathrm{RO}} = 230\,\mathrm{mV}$, and $B = 250\,\mathrm{mT}$. (a) Phase of the reflected rf signal of the left lead $\phi^{\mathrm{L}}_{\mathrm{rf}}$ for varying V_{QD} and V_{H}. (b) Enlargement of (a) for the range indicated by the dashed rectangle. The superimposed text indicates the ground state (GS) of the ABS-QD system in the same basis as in Fig. 3(b). (c) Numerical derivative $d\phi^{\mathrm{L}}_{\mathrm{rf}}/dV_{\mathrm{H}}$ of (b). The superimposed text indicates the parity of the states in (b), where “O” and “E” indicate an odd ground state and an even ground state, respectively. The two crosses indicate negative peaks of $d\phi^{\mathrm{L}}_{\mathrm{rf}}/dV_{\mathrm{H}}$ found from peak-finding for the cut along the diagonal orange line shown in (b). (d) $\phi^{\mathrm{L}}_{\mathrm{rf}}$ for a cut along the orange diagonal line shown in (b). Here V_{QD} and V_{H} are changed in parallel, indicated by δ. The vertical black lines correspond to the V_{QD} and V_{H} values of the black crosses in (c), from which we infer a parity change. The red and blue shading indicate even and odd ground states, respectively.

time τ of 9.3 ms is on the order of quasiparticle poisoning times typically found in hybrid systems, although estimates differ greatly depending on device design [56,57]. This results in the CS predominantly sensing the average occupation of our system. We provide SNRs for different integration times in Appendix H.

III. CONCLUSION

In conclusion, we have operated a QD as a charge sensor and measured the charge of ABSs in a hybrid semiconductor-superconductor nanowire. We have found that the charge of an ABS can change by $2e$ while remaining in the even ground state. The charge difference between the even state and the odd state can be less than $1e$ due to the ABS exchanging charge with the superconductor. We have coupled a QD to an ABS to form a hybridized state, which we categorize as an Andreev molecule. Using the charge sensor, we can infer the parity of the ABS-QD system when the even and odd ground states have different charges. For a two-site Kitaev chain, both parities have the same charge in the sweet spot, and require an additional step for parity-to-charge conversion. We demonstrate that charge sensing can be used to read out parity in hybrid systems—without affecting it—and is promising for use in Kitaev chains.

All raw data in the publication and the analysis code used to generate the figures are available from Ref. [58].

ACKNOWLEDGMENTS

This work was supported by the Dutch Research Council (NWO) and Microsoft Corporation Station Q. We acknowledge useful discussions with Chun-Xiao Liu and Anasua Chatterjee.

D.v.D., G.W., A.B., N.v.L., F.Z., and G.P.M. fabricated the devices. D.v.D. and B.R. performed the electrical measurements. D.v.D., T.D., and B.R. designed the experiment and analyzed the data. D.v.D., T.D., and L.P.K. prepared the manuscript with input from all authors. T.D. and L.P.K. supervised the project.

APPENDIX A: RESONATOR CHARACTERIZATION

Both normal contacts of the device presented in this work are bonded to off-chip LC resonators. Figure 5 shows the amplitude of the reflected rf signal of the left lead $V_{\mathrm{rf}}^{\mathrm{L}}$ and the right lead $V_{\mathrm{rf}}^{\mathrm{R}}$ for varying frequency f at $B = 0$ mT. We fit the resonator responses using a model for asymmetric resonances provided by Khalil *et al.* [59]. From the fit, we obtain the internal and external Q factors listed in Fig. 5. For all other measurements in this work, we fix the frequencies at $f_{\mathrm{L}} = 364$ MHz and $f_{\mathrm{R}} = 264$ MHz. All rf measurements were performed with a Zurich Instruments UHFLI digital lock-in amplifier.

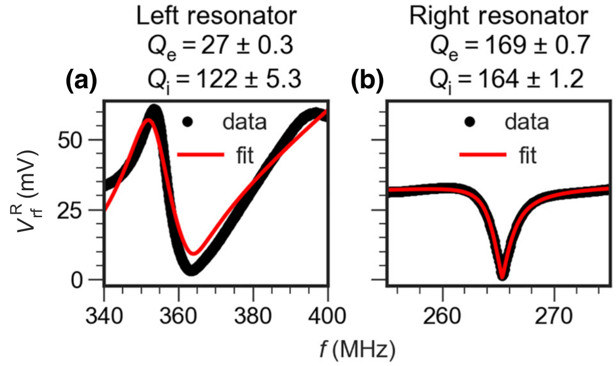

FIG. 5. Resonator characterization. Fits of off-chip resonators performed according to the model described in Ref. [59]. (a) Amplitude of the reflected rf signal of the left lead $V_{\mathrm{rf}}^{\mathrm{L}}$ versus the frequency of the rf output signal f. (b) Amplitude of the reflected rf signal of the right lead $V_{\mathrm{rf}}^{\mathrm{R}}$ versus the frequency of the rf output signal f.

APPENDIX B: VIRTUAL GATES AND FIG. 1 DATA PROCESSING

Figure 6 shows the gates and cross-capacitance matrix $\hat{C}$ used for the virtual gates in this work. The matrix $\hat{C}$ allows us to estimate the actual electrochemical potential change

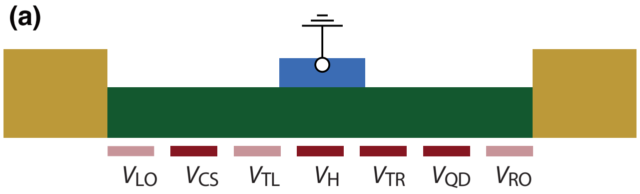

(b)

$$\hat{C} = \begin{array}{ccccc} V_{\mathrm{H}} & V_{\mathrm{CS}} & V_{\mathrm{TR}} & V_{\mathrm{QD}} & \\ 1 & -0.0145 & 0 & 0 & V_{\mathrm{H}} \\ -0.0145 & 1 & 0 & 0 & V_{\mathrm{CS}} \\ 0 & 0 & 1 & -0.5 & V_{\mathrm{TR}} \\ 0 & 0 & -0.5 & 1 & V_{\mathrm{QD}} \end{array}$$

(c)

$$\hat{C} = \begin{array}{cccc} V_{\mathrm{H}} & V_{\mathrm{CS}} & V_{\mathrm{QD}} & \\ 1 & -0.0145 & -0.001 & V_{\mathrm{H}} \\ -0.0145 & 1 & 0 & V_{\mathrm{CS}} \\ -0.001 & 0 & 1 & V_{\mathrm{QD}} \end{array}$$

FIG. 6. Virtual gates. (a) Device sketch that highlights the physical gates used to define the new virtual gates. (b) Cross-capacitance matrix for the gates highlighted in (a). Off-diagonal numbers indicate a finite cross-coupling between physical gates, which is corrected for with use of the virtual gates. This setting is used for Figs. 1 and 2. (c) Same as (b) but corresponding to the data from Fig. 4.

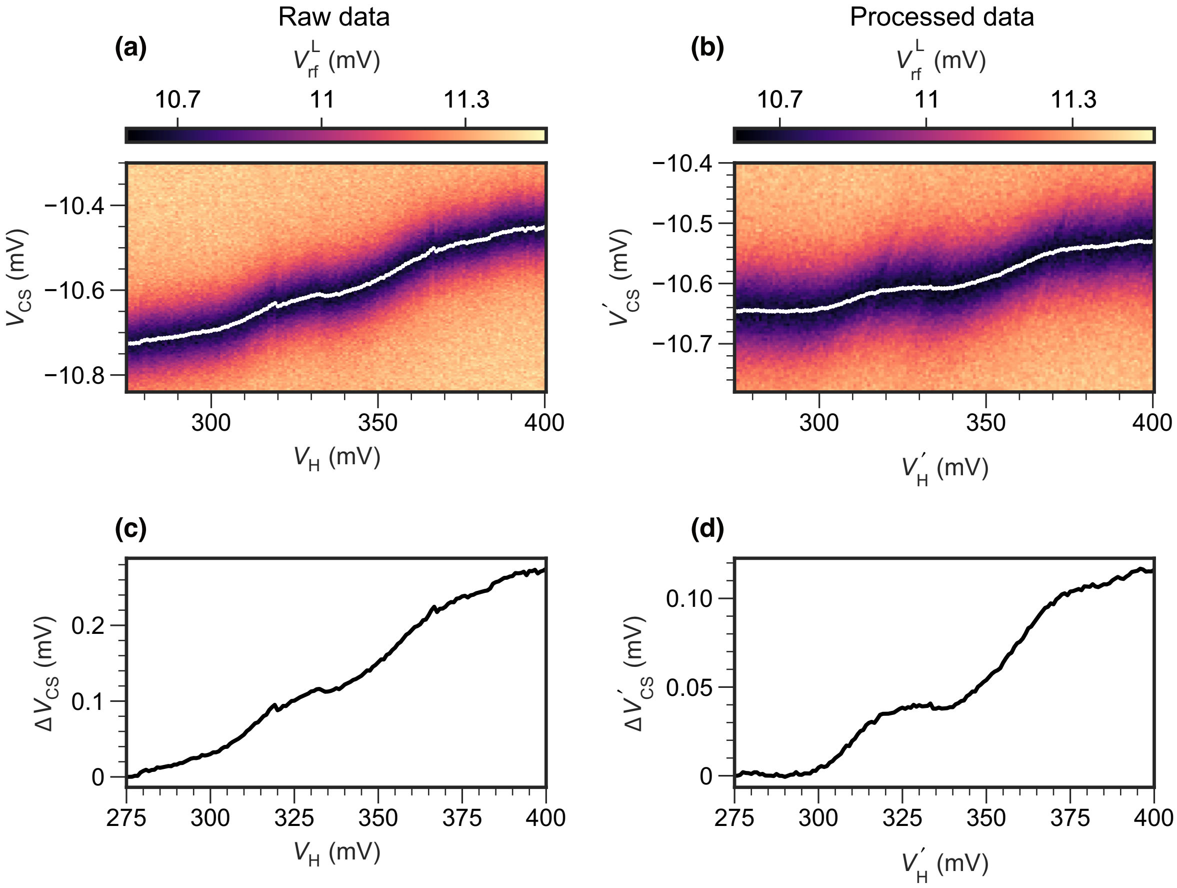

FIG. 7. Data processing of Fig. 1. (a) Amplitude of the reflected rf signal of the left lead V_{rf}^{L} for varying V_{CS} and V_H. White markers indicate the minimum of the Coulomb resonance for each V_H value. (b) Same as (a) but after removal of a global slope between V_{CS} and V_H. (c),(d) Shift of the CS Coulomb resonance ΔV_{CS} for each V_H setting, extracted from (a),(b), respectively. The black lines in (c),(d) correspond to the white lines in (a),(b). The line in (d) is superimposed on the plot in Fig. 1(c).

due to cross-capacitance using $\vec{V}' = \hat{C}\vec{V}$. Here, the vector $\vec{V}$ contains all the physical gate voltages and $\vec{V}'$ is the resulting voltage on parts of the device. This allows us to change gates in a way that, for example, affects only the QD and not the CS electrochemical potential. For more details on virtual gates, see Refs. [60,61].

Our virtual gate implementation was imperfect, leading to a residual cross-capacitance between V_H and V_{CS}. Figure 7(a) shows that the CS resonance is also gated by V_H. We attribute the residual cross-coupling to the nonlinearity of the device and an inaccurate choice of $\hat{C}$. We correct for this in postprocessing by subtracting a global slope until the CS resonance does not depend on V_H up to $V_H = 300$ mV. This result is presented in Figs. 1(e) and 7(b). In Fig. 7(d) we show the minima of the Coulomb dip for each V_H value, extracted from Figs. 7(a) and 7(b) The processed data are seen to be devoid of a global slope. The line in Fig. 6(d) is superimposed on the plot in Fig. 1(c).

APPENDIX C: CHARGE JUMPS

In Fig. 1(c), there is a switch in the tunnel spectroscopy measurement of the hybrid segment at $V_H \approx 365$ mV, which is also observed in Fig. 8(a). These abrupt switches are referred to as "charge jumps," and are attributed to the filling and emptying of charge traps in the nanowire in the vicinity of the ABS. This changes the electrochemical potential of the ABS, which leads to a change in excitation energy as seen in Fig. 1(c). Charge jumps have been observed at reproducible gate voltages in semiconductor-superconductor nanowire devices [62,63].

We attribute the switches in the charge sensor signal in Fig. 1(e) to the emptying and filling of charge traps in the hybrid segment as well. As the electrochemical potential of the ABS changes due to a charge jump, so does its average charge in the singlet ground state. The Coulomb resonance of the charge sensor will shift abruptly as a result. We note that as the change in ABS charge is a fraction of $1e$, the shift of the charge sensor will be comparatively small.

APPENDIX D: EXTENDED-RANGE HYBRID SPECTRUM AND CHARGE SENSING

Figure 8(a) shows the spectrum of the hybrid for a larger range of V_{H} than shown in Fig. 1(c). The ABSs shown in Fig. 1 are indicated by the blue marks. The ABS of Fig. 2 is indicated by the white marks. Figure 8(b) shows the corresponding charge sensor measurement.

APPENDIX E: FIG. 2 CHARGE SENSOR DATA PROCESSING

A change of the ABS charge results in a linear shift of the CS electrochemical potential, proportional to their mutual capacitance. The resulting change in reflected signal $V_{\mathrm{rf}}^{\mathrm{L}}$ is not linear due to the shape of the Coulomb dip. To compensate for this, we first perform a characterization measurement of $V_{\mathrm{rf}}^{\mathrm{L}}$ for varying V_{CS} for each B value as shown in Figs. 9(a)–9(g). We then fix the V_{CS} gate value such that the CS is on Coulomb resonance and measure $V_{\mathrm{rf}}^{\mathrm{L}}$ while varying V_{H}, which is shown in Figs. 9(h)–9(n). For each measured $V_{\mathrm{rf}}^{\mathrm{L}}$ value per V_{H}, we find the closest $V_{\mathrm{rf}}^{\mathrm{L}}$ value in the characterization measurement. We then map the measured $V_{\mathrm{rf}}^{\mathrm{L}}$ value to V_{CS}, which is indicated by the orange markers in Figs. 9(a)–9(g). Finally, we subtract a global slope from the resulting V_{CS} value that we attribute to remaining cross-capacitance to V_{H} and show the resulting ΔV_{CS} in Figs. 9(o)–9(u). We note that the vertical difference between the three plateaus is now roughly equal, as compared with Figs. 9(h)–9(n). Therefore, we interpret the processed data as being proportional to the ABS charge.

Finally, we see from Figs. 9(a)–9(g) that the noise in $V_{\mathrm{rf}}^{\mathrm{L}}$ is larger for some magnetic field values, such as $B = 300\,\mathrm{mT}$, than for others, such as $B = 250\,\mathrm{mT}$. This noise affects the processed data [Figs. 9(o)–9(u)] mostly for $V_{\mathrm{H}} \approx 275\,\mathrm{mV}$, as the charge sensor is already almost in Coulomb blockade, where the noise is largest. While we are not completely certain of the cause, it has been proposed that magnetic fields can affect charge traps, which changes the charge noise [64].

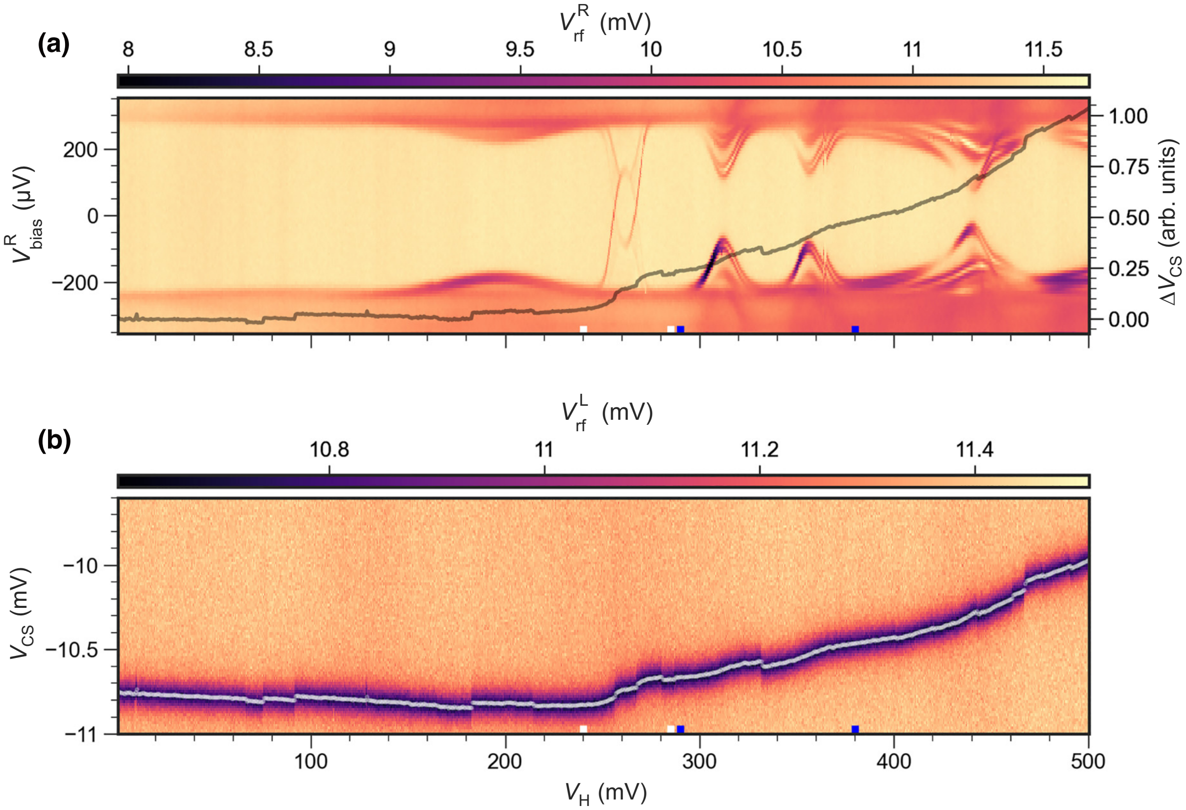

FIG. 8. Extended V_{H} range measurement of Fig. 1. (a) Amplitude of the reflected rf signal of the right lead $V_{\mathrm{rf}}^{\mathrm{R}}$ for varying hybrid gate voltage V_{H} and right bias $V_{\mathrm{bias}}^{\mathrm{R}}$ at $B = 100\,\mathrm{mT}$, $V_{\mathrm{TR}} = 0$, and $V_{\mathrm{RO}} = 500\,\mathrm{mV}$. The superimposed line corresponds to the shift of the CS Coulomb resonance for each V_{H} setting, extracted from (b). A global slope is subtracted for clarity. (b) Amplitude of the reflected rf signal of the left lead $V_{\mathrm{rf}}^{\mathrm{L}}$ for varying V_{CS} and V_{H}. White dots indicate the CS resonance found from peak-finding. The ABSs shown in Fig. 1 are indicated by the blue marks. The ABS of Fig. 2 is indicated by the white marks.

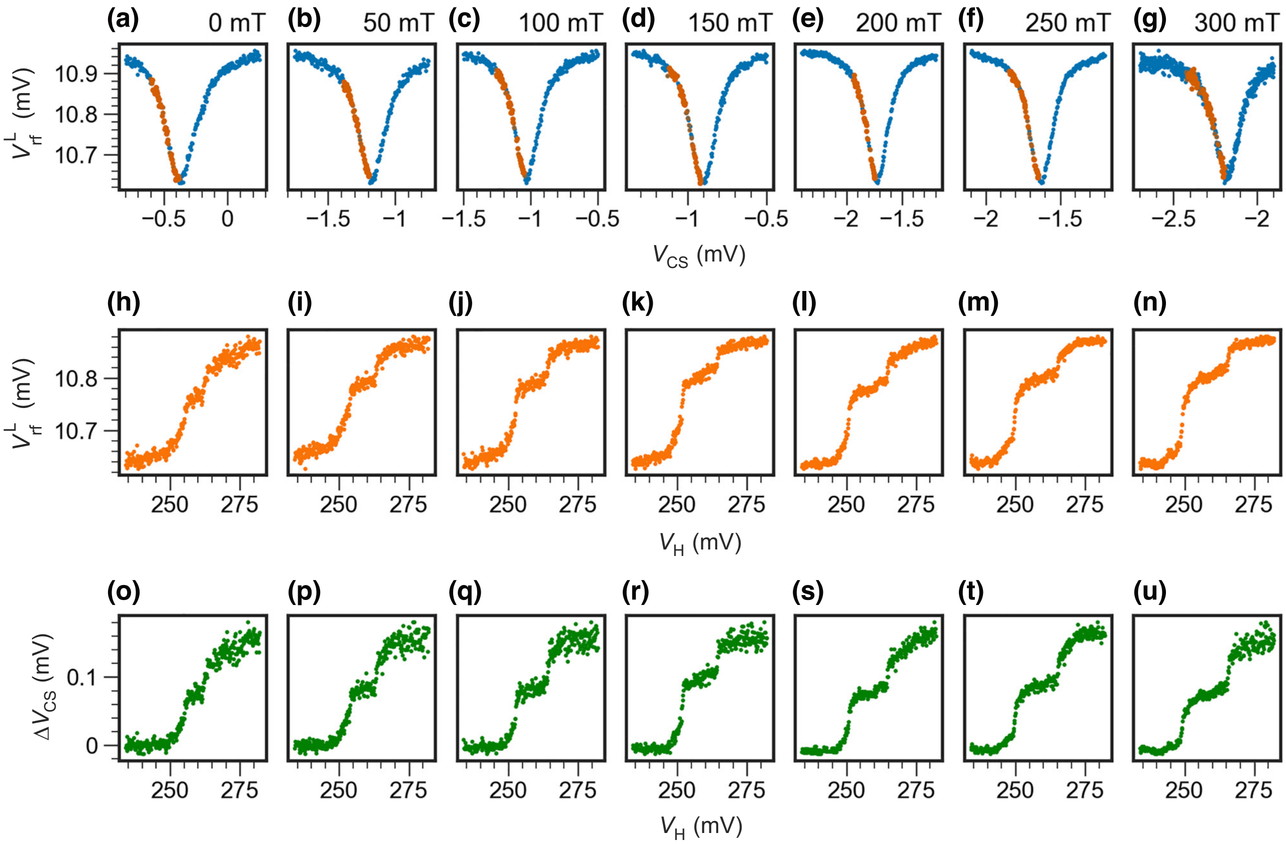

FIG. 9. Data processing of Fig. 2. (a)–(g) Amplitude of the reflected rf signal of the left lead $V^{\mathrm{L}}_{\mathrm{rf}}$ for varying V_{CS} at $V_{\mathrm{H}} = 234$ mV for values of B indicated. These measurements are used to map a measured $V^{\mathrm{L}}_{\mathrm{rf}}$ value to the closest V_{CS} value. Orange markers represent the $V^{\mathrm{L}}_{\mathrm{rf}}$ values from the data shown in (h)–(n), mapped to V_{CS}. For each V_{H} set point, the measured $V^{\mathrm{L}}_{\mathrm{rf}}$ is compared with the full $V^{\mathrm{L}}_{\mathrm{rf}}$ versus V_{CS} curve from (a)–(g). Each measured $V^{\mathrm{L}}_{\mathrm{rf}}$ value from (h)–(n) is then mapped to a V_{CS} value from (a)–(g). (h)–(n) $V^{\mathrm{L}}_{\mathrm{rf}}$ for varying V_{H} at fixed V_{CS} for values of B indicated. At each value of V_{H}, the measured $V^{\mathrm{L}}_{\mathrm{rf}}$ is compared with the corresponding measurement from (a)–(g) for the same value of B. The closest matching value of V_{CS} is then chosen, resulting in a mapping of V_{H} to V_{CS}, which is plotted in orange in (a)–(g). (o)–(u) Shift of the gate voltage corresponding to the Coulomb resonance of the CS ΔV_{CS} for varying V_{H}. The ΔV_{CS} values of the green markers correspond to the V_{CS} values of the orange markers in panels (a)–(g), after subtraction of a global slope.

APPENDIX F: ANDREEV BOUND STATES IN THE ATOMIC LIMIT

The inset in Fig. 2(d) shows the occupation of an ABS modeled in the atomic limit. In the many-body basis of a single orbital $\{|0\rangle, |2\rangle, |{\downarrow}\rangle, |{\uparrow}\rangle\}$ the Hamiltonian is as follows:

$$H_{\mathrm{ABS}} = \begin{bmatrix} 0 & -\Gamma & 0 & 0 \\ -\Gamma & 2\mu + U & 0 & 0 \\ 0 & 0 & \mu + E_Z & 0 \\ 0 & 0 & 0 & \mu - E_Z \end{bmatrix},$$

where μ is the electrochemical potential of the uncoupled orbital, Γ is the coupling to the superconductor, U is the charging energy, and E_Z is the Zeeman energy. We diagonalize the Hamiltonian, obtain the eigenvectors, and calculate the ABS ground state occupation $\langle n\rangle$. For Fig. 2(d), we use $\Gamma = 2.45$, $U = 5$, and $E_Z = 0$, 0.25, or 0.6. For more details on the model, see Refs. [65,66].

For Fig. 3, we combine an atomic-limit ABS with a QD (see Ref. [34] for more details):

$$H = H_{\mathrm{ABS}} + H_{\mathrm{QD}} + H_{\mathrm{t}}, \tag{F1}$$

where for the QD we have

$$H_{\mathrm{QD}} = (\mu_{\mathrm{QD}} - E_Z)c^\dagger_\downarrow c_\downarrow + U_{\mathrm{QD}} c^\dagger_\uparrow c_\uparrow c^\dagger_\downarrow c_\downarrow. \tag{F2}$$

H_{t} describes the tunnel coupling between the ABS and the QD and is given by

$$H_{\mathrm{t}} = t(c^\dagger_\downarrow d_\downarrow + c^\dagger_\uparrow d_\uparrow + \mathrm{H.c.}) + t_{\mathrm{SO}}(-c^\dagger_\downarrow d_\uparrow + c^\dagger_\uparrow d_\downarrow + \mathrm{H.c.}), \tag{F3}$$

where t is the spin-conserving tunneling amplitude and t_{SO} is the spin-flipping tunneling amplitude resulting from spin-orbit interaction.

The basis of Eq. (F1) can be split into even and odd parity subspaces, where we consider the following states in the $|N,M\rangle = |N\rangle_{\mathrm{QD}} \otimes |M\rangle_{\mathrm{ABS}}$ basis:

$$\{|0,S\rangle\,,|2,S\rangle\,,|\downarrow,\downarrow\rangle\} \quad \text{even},$$
$$\{|0,\downarrow\rangle\,,|\downarrow,S\rangle\,,|2,\downarrow\rangle\} \quad \text{odd}.$$

Here $|S\rangle = u\,|0\rangle - v\,|2\rangle$ is the ABS singlet. Using Eq. (F3), we can calculate the effective coupling terms between the basis states of the system. We consider only transitions with a fixed global parity, i.e., only transitions between two odd occupation states or transitions between two even occupation states. The effective coupling between the different even occupation states of the system is given by

$$\langle 2,S|H_t|0,S\rangle = 0, \tag{F4}$$
$$\langle \downarrow,\downarrow|H_t|0,S\rangle = vt_{\mathrm{SO}}, \tag{F5}$$
$$\langle 2,S|H_t|\downarrow,\downarrow\rangle = -ut_{\mathrm{SO}}, \tag{F6}$$

For the odd occupation states we have

$$\langle 0,\downarrow|H_t|\downarrow,S\rangle = ut, \tag{F7}$$
$$\langle 0,\downarrow|H_t|2,\downarrow\rangle = 0, \tag{F8}$$
$$\langle 2,\downarrow|H_t|\downarrow,S\rangle = vt. \tag{F9}$$

We can now write Eq. (F1) in the even and odd parity subspace matrix representation:

$$H_{\mathrm{even}} = \begin{bmatrix} E_{\mathrm{S}} & 0 & vt_{\mathrm{SO}} \\ 0 & 2\mu_{\mathrm{QD}} + U_{\mathrm{QD}} + E_{\mathrm{S}} & -ut_{\mathrm{SO}} \\ vt_{\mathrm{SO}} & -ut_{\mathrm{SO}} & \mu_{\mathrm{QD}} - E_{\mathrm{Z}} + E_{\downarrow} \end{bmatrix}$$

and

$$H_{\mathrm{odd}} = \begin{bmatrix} E_{\downarrow} & ut & 0 \\ ut & \mu_{\mathrm{QD}} - E_{\mathrm{Z}} + E_{\mathrm{S}} & vt \\ 0 & vt & 2\mu_{\mathrm{QD}} + U_{\mathrm{QD}} + E_{\downarrow} \end{bmatrix},$$

where E_{S} and $E_{\downarrow}$ are the ABS singlet and doublet energies, respectively. The full many-body matrix describing the system is given by the following block-diagonal matrix:

$$H_{\mathrm{total}} = \begin{bmatrix} H_{\mathrm{even}} & 0 \\ 0 & H_{\mathrm{odd}} \end{bmatrix}. \tag{F10}$$

The ground state of the system corresponds to the eigenstate of the lowest eigenenergy of Eq. (F10). Figure 3(b) was computed for $U_{\mathrm{ABS}} = 0.03$, $U_{\mathrm{QD}} = 1$, $\Gamma = 0.3$, $E_{\mathrm{Z}} = 0.7$, $t = 0.15$, and $t_{\mathrm{SO}} = 0.01$.

APPENDIX G: FIG. 3 dc TRANSPORT AND rf REFLECTOMETRY COMPARISON

In Fig. 10 we compare the charge stability diagram in Fig. 3(a) as measured by rf reflectometry and dc transport. Most of the features seen in Fig. 10(a) are also seen in Fig. 10(b). Some features are more visible in rf reflectometry measurements than in dc transport. While there is only a finite current when the QD undergoes Andreev reflection or hybridizes with the ABS, there is always a dip in $V_{\mathrm{rf}}^{\mathrm{R}}$ when the normal lead and the QD are on resonance. This can be explained by the excess dissipation known as “Sisyphus resistance,” which originates from the QD level and the Fermi level of the normal lead being detuned with an ac voltage [27]. We attribute the measured current at zero bias in Fig. 10(b) to a finite voltage offset.

APPENDIX H: CHARGE SENSOR SNR

To estimate the SNR of the charge sensor, we measure the in-phase response I and quadrature Q of the left resonator for the ABS of Fig. 2 at $B = 100\,\mathrm{mT}$. We measure the I and Q signals over time at different V_{H} values and plot the result in histograms, as shown in Fig. 11(a). For each histogram, we compute the average in-phase and quadrature response μ_i and the standard deviation σ_i. Then we define the SNR for two charge states as

$$\mathrm{SNR}_{i,j} = \frac{|\mu_i - \mu_j|}{\sigma_i + \sigma_j};$$

see supplemental material in Ref. [67] for details. The red and purple lines in Fig. 11(a) show $|\mu_i - \mu_j|$ for the 0 and 1 and for the 1 and 2 occupations of the ABS. Division by the sum of the standard deviations results in the SNR.

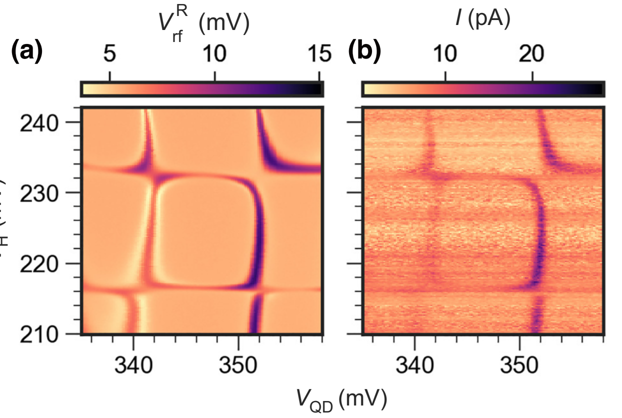

FIG. 10. Comparison of dc transport and rf reflectometry in Fig. 3 at $V_{\mathrm{bias}}^{\mathrm{R}} = 0$. (a) Amplitude of the reflected rf signal of the right lead $V_{\mathrm{rf}}^{\mathrm{R}}$ for varying QD plunger gate voltage V_{QD} and V_{H}. (b) Current measured at the right lead I for varying QD plunger gate voltage V_{QD} and V_{H}.

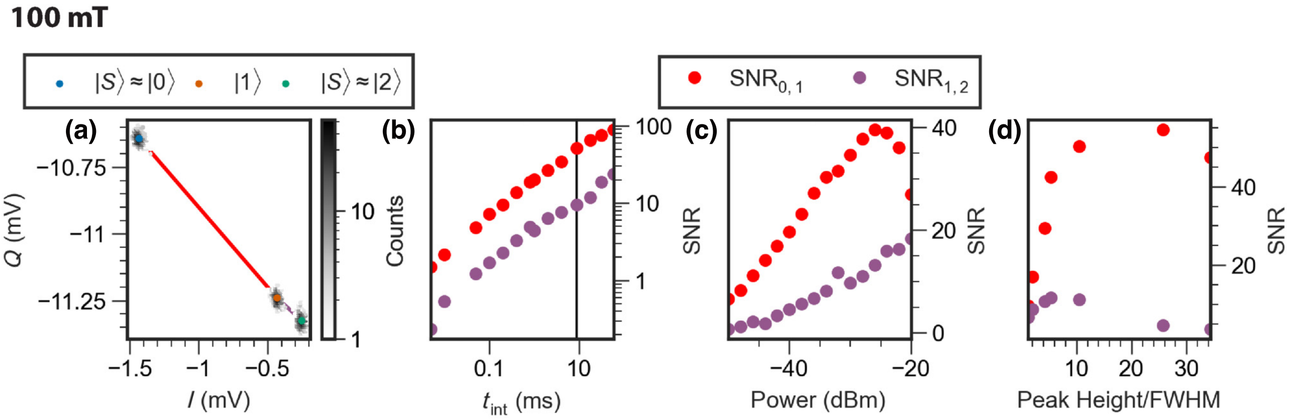

FIG. 11. Charge sensor SNR measurements for a single ABS. (a) Example histograms of the in-phase response I and quadrature Q of the left resonator for the 0-like even, 1, and 2-like even occupations of the ABS. The colored markers indicate the charge state of the ABS that corresponds to each histogram. The red and purple lines show the distance between the histograms that we use to calculate the SNR. (b) The SNR calculated from in-phase and quadrature histograms for the 0-like singlet and doublet states (red) and the 2-like singlet and doublet states (purple) for varying integration time t_{int}. The vertical black line indicates $t_{\text{int}} = 9.3$ ms, which is the integration time used in the main text. The rf output signal had a power of −30 dBm for every t_{int}. (c) Same as (b) but for varying power of the rf input signal and at fixed $t_{\text{int}} = 9.3$ ms. (d) Same as (c) but for varying shape of the CS Coulomb resonance at fixed $t_{\text{int}} = 9.3$ ms and power −30 dBm. Each data point is recorded for a different gate voltage V_{LO}, resulting in Coulomb peaks of different width. We present the SNR versus Coulomb peak height divided by the full width at half maximum (FWHM).

Figure 11(b) shows the SNR calculated for varying integration time t_{int}. Figure 11(c) shows the SNR calculated for varying rf output power. It reaches a maximum of 39.5 for −26 dBm for the SNR of the 0-like singlet and 1 occupations. Figure 11(d) shows the SNR calculated for varying tunnel gate voltage V_{LO}. We fit the resulting Coulomb peak and extract the ratio of the peak height and full width at half maximum. We see that a sharper Coulomb peak results in a higher SNR.

[1] A. Y. Kitaev, Unpaired Majorana fermions in quantum wires, Physics-Uspekhi **44**, 131 (2001).

[2] Y. Oreg, G. Refael, and F. von Oppen, Helical liquids and Majorana bound states in quantum wires, Phys. Rev. Lett. **105**, 177002 (2010).

[3] R. M. Lutchyn, J. D. Sau, and S. Das Sarma, Majorana fermions and a topological phase transition in semiconductor-superconductor heterostructures, Phys. Rev. Lett. **105**, 077001 (2010).

[4] J. D. Sau and S. D. Sarma, Realizing a robust practical Majorana chain in a quantum-dot-superconductor linear array, Nat. Commun. **3**, 964 (2012).

[5] I. C. Fulga, A. Haim, A. R. Akhmerov, and Y. Oreg, Adaptive tuning of Majorana fermions in a quantum dot chain, New J. Phys. **15**, 045020 (2013).

[6] M. Leijnse and K. Flensberg, Parity qubits and poor man's Majorana bound states in double quantum dots, Phys. Rev. B. **86**, 134528 (2012).

[7] C.-X. Liu, G. Wang, T. Dvir, and M. Wimmer, Tunable superconducting coupling of quantum dots via Andreev bound states in semiconductor-superconductor nanowires, Phys. Rev. Lett. **129**, 267701 (2022).

[8] A. Tsintzis, R. S. Souto, and M. Leijnse, Creating and detecting poor man's Majorana bound states in interacting quantum dots, Phys. Rev. B **106**, L201404 (2022).

[9] T. Dvir, G. Wang, N. Van Loo, C.-X. Liu, G. P. Mazur, A. Bordin, S. L. D. Ten Haaf, J.-Y. Wang, D. Van Driel, F. Zatelli, X. Li, F. K. Malinowski, S. Gazibegovic, G. Badawy, E. P. A. M. Bakkers, M. Wimmer, and L. P. Kouwenhoven, Realization of a minimal Kitaev chain in coupled quantum dots, Nature **614**, 445 (2023).

[10] P. Boross and A. Pályi, Braiding-based quantum control of a Majorana qubit built from quantum dots, ArXiv:2305.08464 (2023).

[11] C.-X. Liu, H. Pan, F. Setiawan, M. Wimmer, and J. D. Sau, Fusion protocol for Majorana modes in coupled quantum dots, ArXiv:2212.01653 (2022).

[12] L. C. Contamin, M. R. Delbecq, B. Douçot, A. Cottet, and T. Kontos, Hybrid light-matter networks of Majorana zero modes, npj Quantum Inf. **7**, 171 (2021).

[13] M. Hinderling, S. C. t. Kate, D. Z. Haxell, M. Coraiola, S. Paredes, E. Cheah, F. Krizek, R. Schott, W. Wegscheider, D. Sabonis, and F. Nichele, Flip-chip-based fast inductive parity readout of a planar superconducting island, ArXiv:2307.06718 (2023).

[14] S. Plugge, A. Rasmussen, R. Egger, and K. Flensberg, Majorana box qubits, New J. Phys. **19**, 012001 (2017).

[15] D. Aasen, M. Hell, R. V. Mishmash, A. Higginbotham, J. Danon, M. Leijnse, T. S. Jespersen, J. A. Folk, C. M. Marcus, K. Flensberg, and J. Alicea, Milestones toward Majorana-based quantum computing, Phys. Rev. X **6**, 031016 (2016).

[16] G. Széchenyi and A. Pályi, Parity-to-charge conversion for readout of topological Majorana qubits, Phys. Rev. B **101**, 235441 (2020).

[17] D. Sabonis, D. van Zanten, J. Suter, T. Karzig, D. I. Pikulin, J. I. Väyrynen, E. O'Farrell, D. Razmadze,

P. Krogstrup, and C. M. Marcus, Comparing tunneling spectroscopy and charge sensing of Andreev bound states in a semiconductor-superconductor hybrid nanowire structure, ArXiv:2105.08871 (2021).

[18] D. Razmadze, D. Sabonis, F. K. Malinowski, G. C. Ménard, S. Pauka, H. Nguyen, D. M. van Zanten, E. C. O'Farrell, J. Suter, P. Krogstrup, F. Kuemmeth, and C. M. Marcus, Radio-frequency methods for Majorana-based quantum devices: Fast charge sensing and phase-diagram mapping, Phys. Rev. Appl. **11**, 064011 (2019).

[19] S. Heedt, M. Quintero-Pérez, F. Borsoi, A. Fursina, N. van Loo, G. P. Mazur, M. P. Nowak, M. Ammerlaan, K. Li, S. Korneychuk, J. Shen, M. A. Y. van de Poll, G. Badawy, S. Gazibegovic, N. de Jong, P. Aseev, K. van Hoogdalem, E. P. A. M. Bakkers, and L. P. Kouwenhoven, Shadow-wall lithography of ballistic superconductor–semiconductor quantum devices, Nat. Commun. **12**, 4914 (2021).

[20] D. van Driel, G. Wang, A. Bordin, N. van Loo, F. Zatelli, G. P. Mazur, D. Xu, S. Gazibegovic, G. Badawi, E. P. A. M. Bakkers, L. P. Kouwenhoven, and T. Dvir, Spin-filtered measurements of Andreev bound states in semiconductor-superconductor nanowire devices, Nat. Commun. **14**, 6880 (2023).

[21] M. House, I. Bartlett, P. Pakkiam, M. Koch, E. Peretz, J. van der Heijden, T. Kobayashi, S. Rogge, and M. Simmons, High-sensitivity charge detection with a single-lead quantum dot for scalable quantum computation, Phys. Rev. Appl. **6**, 044016 (2016).

[22] J. M. Hornibrook, J. I. Colless, A. C. Mahoney, X. G. Croot, S. Blanvillain, H. Lu, A. C. Gossard, and D. J. Reilly, Frequency multiplexing for readout of spin qubits, Appl. Phys. Lett. **104**, 103108 (2014).

[23] J.-Y. Wang, N. van Loo, G. P. Mazur, V. Levajac, F. K. Malinowski, M. Lemang, F. Borsoi, G. Badawy, S. Gazibegovic, E. P. A. M. Bakkers, M. Quintero-Pérez, S. Heedt, and L. P. Kouwenhoven, Parametric exploration of zero-energy modes in three-terminal InSb-Al nanowire devices, Phys. Rev. B **106**, 075306 (2022).

[24] A. Assouline, C. Feuillet-Palma, A. Zimmers, H. Aubin, M. Aprili, and J.-C. Harmand, Shiba bound states across the mobility edge in doped InAs nanowires, Phys. Rev. Lett. **119**, 097701 (2017).

[25] J. Barański and T. Domański, In-gap states of a quantum dot coupled between a normal and a superconducting lead, J. Phys.: Condens. Matter **25**, 435305 (2013).

[26] E. J. H. Lee, X. Jiang, M. Houzet, R. Aguado, C. M. Lieber, and S. De Franceschi, Spin-resolved Andreev levels and parity crossings in hybrid superconductor–semiconductor nanostructures, Nat. Nanotechnol. **9**, 79 (2014).

[27] F. Persson, C. M. Wilson, M. Sandberg, G. Johansson, and P. Delsing, Excess dissipation in a single-electron box: The Sisyphus resistance, Nano Lett. **10**, 953 (2010).

[28] L. DiCarlo, H. J. Lynch, A. C. Johnson, L. I. Childress, K. Crockett, C. M. Marcus, M. P. Hanson, and A. C. Gossard, Differential charge sensing and charge delocalization in a tunable double quantum dot, Phys. Rev. Lett. **92**, 226801 (2004).

[29] Y. Hu, H. O. H. Churchill, D. J. Reilly, J. Xiang, C. M. Lieber, and C. M. Marcus, A Ge/Si heterostructure nanowire-based double quantum dot with integrated charge sensor, Nat. Nanotechnol. **2**, 622 (2007).

[30] M. Deng, S. Vaitiekėnas, E. B. Hansen, J. Danon, M. Leijnse, K. Flensberg, J. Nygård, P. Krogstrup, and C. M. Marcus, Majorana bound state in a coupled quantum-dot hybrid-nanowire system, Science **354**, 1557 (2016).

[31] M. Valentini, F. Peñaranda, A. Hofmann, M. Brauns, R. Hauschild, P. Krogstrup, P. San-Jose, E. Prada, R. Aguado, and G. Katsaros, Nontopological zero-bias peaks in full-shell nanowires induced by flux-tunable Andreev states, Science **373**, 82 (2021).

[32] J. Danon, A. B. Hellenes, E. B. Hansen, L. Casparis, A. P. Higginbotham, and K. Flensberg, Nonlocal conductance spectroscopy of Andreev bound states: Symmetry relations and BCS charges, Phys. Rev. Lett. **124**, 036801 (2020).

[33] G. C. Ménard, G. L. R. Anselmetti, E. A. Martinez, D. Puglia, F. K. Malinowski, J. S. Lee, S. Choi, M. Pendharkar, C. J. Palmstrøm, K. Flensberg, C. M. Marcus, L. Casparis, and A. P. Higginbotham, Conductance-matrix symmetries of a three-terminal hybrid device, Phys. Rev. Lett. **124**, 036802 (2020).

[34] S. Miles, D. van Driel, M. Wimmer, and C.-X. Liu, Kitaev chain in an alternating quantum dot-Andreev bound state array, ArXiv:2309.15777 (2023).

[35] W. Samuelson, V. Svensson, and M. Leijnse, Minimal quantum dot based Kitaev chain with only local superconducting proximity effect, Phys. Rev. B **109**, 035415 (2024).

[36] L. Yu, Bound state in superconductors with paramagnetic impurities, Acta Phys. Sin. **21**, 75 (1965).

[37] H. Shiba, Classical spins in superconductors, Prog. Theor. Phys. **40**, 435 (1968).

[38] A. Rusinov, Superconductivity near a paramagnetic impurity, JETP Lett. **9**, 85 (1969).

[39] K. Grove-Rasmussen, H. I. Jørgensen, B. M. Andersen, J. Paaske, T. S. Jespersen, J. Nygård, K. Flensberg, and P. E. Lindelof, Superconductivity-enhanced bias spectroscopy in carbon nanotube quantum dots, Phys. Rev. B **79**, 134518 (2009).

[40] A. Jellinggaard, K. Grove-Rasmussen, M. H. Madsen, and J. Nygård, Tuning Yu-Shiba-Rusinov states in a quantum dot, Phys. Rev. B **94**, 064520 (2016).

[41] G. O. Steffensen, J. C. E. Saldaña, A. Vekris, P. Krogstrup, K. Grove-Rasmussen, J. Nygård, A. L. Yeyati, and J. Paaske, Direct transport between superconducting subgap states in a double quantum dot, Phys. Rev. B **105**, L161302 (2022).

[42] Z. Su, A. B. Tacla, M. Hocevar, D. Car, S. R. Plissard, E. P. A. M. Bakkers, A. J. Daley, D. Pekker, and S. M. Frolov, Andreev molecules in semiconductor nanowire double quantum dots, Nat. Commun. **8**, 585 (2017).

[43] O. Kürtössy, Z. Scherübl, G. Fülöp, I. E. Lukács, T. Kanne, J. Nygård, P. Makk, and S. Csonka, Andreev molecule in parallel InAs nanowires, Nano Lett. **21**, 7929 (2021).

[44] Z. Scherübl, A. Pályi, and S. Csonka, Transport signatures of an Andreev molecule in a quantum dot–superconductor–quantum dot setup, Beilstein J. Nanotechnol. **10**, 363 (2019).

[45] J. C. Estrada Saldaña, A. Vekris, R. Žitko, G. Steffensen, P. Krogstrup, J. Paaske, K. Grove-Rasmussen, and J. Nygård, Two-impurity Yu-Shiba-Rusinov states in coupled quantum dots, Phys. Rev. B **102**, 195143 (2020).

[46] K. Grove-Rasmussen, G. Steffensen, A. Jellinggaard, M. H. Madsen, R. Žitko, J. Paaske, and J. Nygård, Yu–Shiba–Rusinov screening of spins in double quantum dots, Nat. Commun. **9**, 2376 (2018).

[47] H. Potts, M. Aspegren, R. Debbarma, S. Lehmann, and C. Thelander, Large-bias spectroscopy of Yu-Shiba-Rusinov states in a double quantum dot, Nanotechnology **34**, 135002 (2023).

[48] D. Z. Haxell, M. Coraiola, M. Hinderling, S. C. t. Kate, D. Sabonis, A. E. Svetogorov, W. Belzig, E. Cheah, F. Krizek, R. Schott, W. Wegscheider, and F. Nichele, Demonstration of nonlocal Josephson effect in Andreev molecules, ArXiv:2306.00866 (2023).

[49] M. Coraiola, D. Z. Haxell, D. Sabonis, H. Weisbrich, A. Svetogorov, M. Hinderling, S. C. ten Kate, E. Cheah, F. Krizek, R. Schott, *et al.*, Hybridisation of Andreev bound states in three-terminal josephson junctions, ArXiv:2302.14535 (2023).

[50] M. Kocsis, Z. Scherübl, G. Fülöp, P. Makk, and S. Csonka, Strong nonlocal tuning of the current-phase relation of a quantum dot based Andreev molecule, ArXiv:2303.14842 (2023).

[51] E. Prada, R. Aguado, and P. San-Jose, Measuring Majorana nonlocality and spin structure with a quantum dot, Phys. Rev. B **96**, 085418 (2017).

[52] D. J. Clarke, Experimentally accessible topological quality factor for wires with zero energy modes, Phys. Rev. B **96**, 201109 (2017).

[53] A. Pöschl, A. Danilenko, D. Sabonis, K. Kristjuhan, T. Lindemann, C. Thomas, M. J. Manfra, and C. M. Marcus, Nonlocal signatures of hybridization between quantum dot and Andreev bound states, Phys. Rev. B **106**, L161301 (2022).

[54] J. R. Petta, A. C. Johnson, J. M. Taylor, E. A. Laird, A. Yacoby, M. D. Lukin, C. M. Marcus, M. P. Hanson, and A. C. Gossard, Coherent manipulation of coupled electron spins in semiconductor quantum dots, Science **309**, 2180 (2005).

[55] A. Tsintzis, R. S. Souto, K. Flensberg, J. Danon, and M. Leijnse, Roadmap towards Majorana qubits and nonabelian physics in quantum dot-based minimal Kitaev chains, ArXiv:2306.16289 (2023).

[56] W. Uilhoorn, J. G. Kroll, A. Bargerbos, S. D. Nabi, C.-K. Yang, P. Krogstrup, L. P. Kouwenhoven, A. Kou, and G. de Lange, Quasiparticle trapping by orbital effect in a hybrid superconducting-semiconducting circuit, ArXiv:2105.11038 (2021).

[57] A. Bargerbos, M. Pita-Vidal, J. Ávila, L. J. Splitthoff, L. Grünhaupt, J. J. Wesdorp, C. K. Andersen, Y. Liu, L. P. Kouwenhoven, R. Aguado, *et al.*, Singlet-doublet transitions of a quantum dot Josephson junction detected in a transmon circuit, PRX Quantum **3**, 030311 (2022).

[58] https://doi.org/10.5281/zenodo.10067038.

[59] M. S. Khalil, M. J. A. Stoutimore, F. C. Wellstood, and K. D. Osborn, An analysis method for asymmetric resonator transmission applied to superconducting devices, J. Appl. Phys. **111**, 054510 (2012).

[60] C. Volk, A. M. J. Zwerver, U. Mukhopadhyay, P. T. Eendebak, C. J. van Diepen, J. P. Dehollain, T. Hensgens, T. Fujita, C. Reichl, W. Wegscheider, and L. M. K. Vandersypen, Loading a quantum-dot based “Qubyte” register, npj Quantum Inf. **5**, 1 (2019).

[61] A. R. Mills, D. M. Zajac, M. J. Gullans, F. J. Schupp, T. M. Hazard, and J. R. Petta, Shuttling a single charge across a one-dimensional array of silicon quantum dots, Nat. Commun. **10**, 1063 (2019).

[62] F. Luthi, T. Stavenga, O. Enzing, A. Bruno, C. Dickel, N. Langford, M. A. Rol, T. S. Jespersen, J. Nygård, P. Krogstrup, *et al.*, Evolution of nanowire transmon qubits and their coherence in a magnetic field, Phys. Rev. Lett. **120**, 100502 (2018).

[63] H. Zheng, L. Y. Cheung, N. Sangwan, A. Kononov, R. Haller, J. Ridderbos, C. Ciaccia, J. H. Ungerer, A. Li, E. P. Bakkers, *et al.*, Coherent control of a few-channel hole type gatemon qubit, ArXiv:2312.06411 (2023).

[64] S. M. Albrecht, A. P. Higginbotham, M. Madsen, F. Kuemmeth, T. S. Jespersen, J. Nygård, P. Krogstrup, and C. Marcus, Exponential protection of zero modes in Majorana islands, Nature **531**, 206 (2016).

[65] J. Bauer, A. Oguri, and A. C. Hewson, Spectral properties of locally correlated electrons in a Bardeen–Cooper–Schrieffer superconductor, J. Phys.: Condens. Matter **19**, 486211 (2007).

[66] A. Martín-Rodero and A. L. Yeyati, The Andreev states of a superconducting quantum dot: Mean field versus exact numerical results, J. Phys.: Condens. Matter **24**, 385303 (2012).

[67] D. de Jong, C. G. Prosko, D. M. A. Waardenburg, L. Han, F. K. Malinowski, P. Krogstrup, L. P. Kouwenhoven, J. V. Koski, and W. Pfaff, Rapid microwave-only characterization and readout of quantum dots using multiplexed gigahertz-frequency resonators, Phys. Rev. Appl. **16**, 014007 (2021).